Soft Matter

Dynamics of non-Brownian fiber suspensions under periodic shear

SCHOLARONE™
Manuscripts

ARTICLE TYPE

Dynamics of non-Brownian fiber suspensions under periodic shear

Alexandre Franceschini,[a] **Emmanouela Filippidi,**[a] **Elisabeth Guazzelli,**[b] **and David J. Pine**[*a,c]

We report experiments studying the dynamics of dense non-Brownian fiber suspensions subjected to periodic oscillatory shear. We find that periodic shear initially causes fibers to collide and to undergo irreversible diffusion. As time progresses, the fibers tend to orient in the vorticity direction while the number of collisions decreases. Ultimately, the system goes to one of two steady states: an absorbing steady state, where collisions cease and the fibers undergo reversible trajectories; an active state, where fibers continue to collide causing them to diffuse and undergo irreversible trajectories. Collisions between fibers can be characterized by an effective volume fraction Φ with a critical volume fraction Φ_c that separates absorbing from active (diffusing) steady states. The effective volume fraction Φ depends on the mean fiber orientation and thus decreases in time as fibers progressively orient under periodic shear. In the limit that the temporal evolution of Φ is slow compared to the activity relaxation time τ, all the data for all strain amplitudes and all concentrations can be scaled onto a single master curve with a functional dependence well-described by $t_R^{-\beta/\nu} e^{-t_R}$, where t_R is the rescaled time. As $\Phi \to \Phi_c$, τ diverges. Therefore, for experiments in which $\Phi(t)$ starts above Φ_c but goes to a steady state below Φ_c, departures from scaling are observed for Φ very near Φ_c. The critical exponents are measured to be $\beta = 0.84 \pm 0.04$ and $\nu = 1.1 \pm 0.1$, which is consistent with the Manna universality class for directed percolation.

1 Introduction

The collective organization of athermal rods suspended in a liquid is relevant for several fields of engineering and science, including oil extraction,[1] cement reinforcement,[2] and blood flows.[3,4] While the rheology of suspensions of athermal rods is reasonably well studied,[5,6] the mechanisms controlling particle organization remain unclear, especially at high concentration, where collisions dominate structural reorganization.[7–9] In contrast to colloidal suspensions, which are driven by thermal forces towards a free energy minimum, athermal suspensions lack a general theoretical framework to explain their collective organization.[10,11] Based on the present study of concentrated suspensions of athermal non-colloidal fibers under periodic shear, we suggest that the dynamics of non-colloidal fibers in suspension can be understood as a directed percolation process,[10] controlled by a slowly relaxing *effective volume fraction* that quantifies the probability of shear-induced collisions.

At low Reynolds numbers, hydrodynamic interactions are expected to be reversible.[12] However, experiments and simulations on suspensions of spheres[13–17] and fibers[18–23] show that there are circumstances where simple hydrodynamic reversibility seems to be violated. Under slow periodic shear, some particles trace out periodic trajectories, but a fraction of particles undergo small random displacements,[14,16] which are believed to be induced by non-hydrodynamic interactions that arise during particle collisions.[13,14,16,17,22] Particles that undergo irreversible displacements are said to be *active*; their irreversible motion under periodic shear leads to particle diffusion.[13] For randomly prepared systems, this diffusion is observed to slowly diminish with time as particles find positions that reduce the probability of collision. If the strain amplitude is sufficiently small, complete reversibility is achieved. Above a volume-fraction-dependent strain threshold, however, full reversibility is not achieved and a steady state develops in which a finite fraction of particles undergo random displacements and diffusion persists.[15,22,24]

The transition between a quiescent *absorbing* state with no active particles and a *fluctuating* state is a non-equilibrium critical phase transition called an *absorbing phase transition* (APT).[10,25,26] It has been observed in other driven systems with a conserved number of particles, including simulated systems such as sandpiles[25] and experimental systems such as superconducting vortices.[27] It belongs to a broader class of transitions called conserved directed percolation (CDP, or the Manna class),[10,17] whose basic physics is captured by the *random organization* model.[15] In this model, particles are subjected to an oscillatory shear and experience random displacements if they come within a specified distance of each other.[17]

---

a Center for Soft Matter Research, Department of Physics, New York University, 4 Washington Place, New York, NY 10003, USA; E-mail: pine@nyu.edu
b Aix-Marseille Université, CNRS, IUSTI UMR 7343, 5 rue Enrico Fermi, 13453 Marseille Cedex 13, France
c Department of Chemical & Biomolecular Engineering, Polytechnic School of Engineering, New York University, 6 MetroTech Center, Brooklyn, NY 11201

At low strain amplitude, the system finds an absorbing state after a number of oscillations. At a strain amplitude higher than a volume fraction dependent critical threshold, the effect of close encounters propagates throughout the system, initiating persistent diffusion.[13,17]

In this article, we investigate the absorbing phase transition observed in fiber suspensions under oscillatory shear. By focusing on confined suspensions at several volume fractions, we show that this transition is controlled by a slowly-relaxing parameter, the effective volume fraction, which quantifies the frequency of fiber-fiber collisions under shear. This effective volume fraction is a function of the strain amplitude, the volume fraction and the slowly-relaxing fiber orientation distribution.[22,23] We measure the experimental values of the critical exponents associated with this transition and show that they are consistent with the Manna universality class. This result confirms that fibers and sphere suspension dynamics have the same underlying physics once the orientation distribution is taken into account.

2 Formulation of the Problem

2.1 Description of the experiment

We use the same non-Brownian nylon rods described previously, with length $L = 1.52 \pm 0.14$ mm and diameter $d = 0.140 \pm 0.001$ mm.[22] They have a length-to-diameter ratio $L/d = 11$ and are suspended in a density-matched, highly viscous Newtonian fluid.[15] In this study, the volume fraction c of rods ranges between 0.05 and 0.20. Thus, all concentrations are above the semi-dilute overlap concentration $c^\star = \frac{3}{2}(d/L)^2 = 0.013$ defined by the concentration where spheres of diameter L fill the sample volume. The concentrations straddle the boundary between the semi-dilute and concentrated regimes $c^{\star\star} = d/L = 0.092$, defined by the concentration where disks of diameter L and thickness d fill the sample volume. All concentrations are below the Onsager isotropic-to-nematic concentration $c_{IN} = 3.34(d/L) = 0.31$.

The suspensions are confined in the thin gap $g = 1.5L$ of a transparent Couette cell (Fig. 1b). The refractive index of the fluid and fibers are matched, with a small fraction of the fibers labeled with rhodamine dye to facilitate viewing when illuminated by a sheet of laser light, as described in Fig. 1.

To ensure a reproducible initial state, the sample is sheared at a steady moderate strain rate ($Re \approx 0.1$) before the start of each measurement.[28,29] The total strain applied during this "pre-shear" is on the order of 10^2. The pre-shear is turned off, and then after a few minutes rest (this time is not important), the sample is subjected to periodic strain with a strain by oscillating the inner cylinder. In a typical experiment, the sample is subject to 250 to 1500 shear cycles with a strain amplitude γ and a period of about 30 s, ensuring that the Reynolds
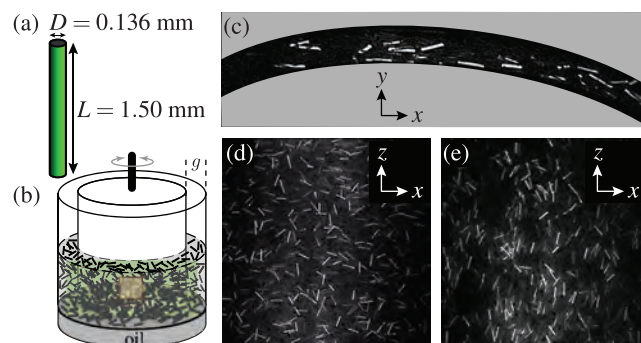

Fig. 1 (a) The fibers are 1.5-mm-long cylinders with a aspect ratio of 11. (b) Couette cell with illuminated with a 532 nm green laser sheet, oriented either vertically or horizontally for viewing either from the side or the top, respectively, of the Couette shear cell. The yellow rectangle shows the observation window when a vertical laser sheet is used. The bottom of the Couette cell, where the shear flow is not homogeneous, is filled with a heavy immiscible fluorinated oil that prevents particles from migrating underneath the rotating central cylinder. (c) x-y projection of the Couette shear cell filled with a suspension at $c = 0.15$. A small fraction ($\approx 5\%$) of the fibers are dyed with Rhodamine and are tracked.[30] These fibers are between L and $3L$ from the liquid-air boundary. (d-e) Images of the dyed fibers in the x-z plane (d) before and (e) after a run at $c = 0.15$ with $\gamma = 2.90$ showing that the fibers tend to align vertically in the vorticity plane after periodically sheared for a period of time. The evolution of the orientation distribution is discussed in the text.

number $Re < 5 \times 10^{-3}$. The samples are typically strained sinusoidally, although using other waveforms—triangular for example—have no apparent affect on the results. Similarly, none of the results depends on the period (or frequency) of oscillation in low Reynolds number regime studied here, that is for $Re \ll 1$.

The positions of the fluorescent fibers, illuminated by the laser sheet, are digitally recorded once each cycle, either from the top (Fig. 1c) or from the side (Fig. 1d-e) of the Couette cell. Fibers that undergo perfectly reversible periodic trajectories appear at the same position and orientation in successive images. Fibers whose trajectories are not reversible appear displaced and/or rotated in successive images. In either case, the center of mass positions and orientations of each fiber are extracted from the images and tracked using standard methods.[30]

In addition to recording the particle coordinates, the complex viscosity is recorded, as the central cylinder in the Couette cell is part of a commercial rheometer, as described previously.[15,22]
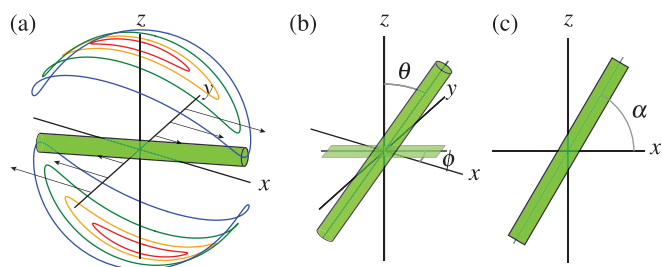
Fig. 2 a: Jeffery orbits with $C = 0.5$ (—), $C = 1$ (—), $C = 2$ (—), $C = 4$ (—). The fiber is shown at an orbit extremum, which is the most probable position. **b**: Representation of a fiber in spherical coordinates, with projection onto x-y plane. **c**: Projection of a fiber onto the x-z plane.

Fig. 3 Temporal evolution of S_ϕ at $c = 0.15$ for selected strain amplitudes. **Inset**: Orientational probability distribution function of ϕ, according to our measurements (■) at $c = 0.15$ and Jeffery equations (—).

2.2 Motion of fibers in shear flow

An isolated cylindrical fiber in a steady homogeneous shear flow undergoes a tumbling motion called a Jeffery orbit.[31,32] It is the composition of a trivial center-of-mass translation with a periodic rotation of the fiber centered about the vorticity axis defined by the flow (Fig. 2a). The fibers used here are cylinders with a constant circular cross section, but can be modeled as ellipsoids with an effective aspect ratio of $r = 0.7L/D$.[9,33] Such a fiber spends a time $\mathcal{O}(r)$ aligned with the flow in the x-z plane (*cf.* Fig. 2a) and rapidly tumbles, flipping head to tail, in a time $\mathcal{O}(1/r)$. The tilt of the fiber from the z axis is related to the orbit constant C: $C \to 0$ corresponds to alignment along the vorticity axis z, while $C \to \infty$ corresponds to rotation in the x-y plane.
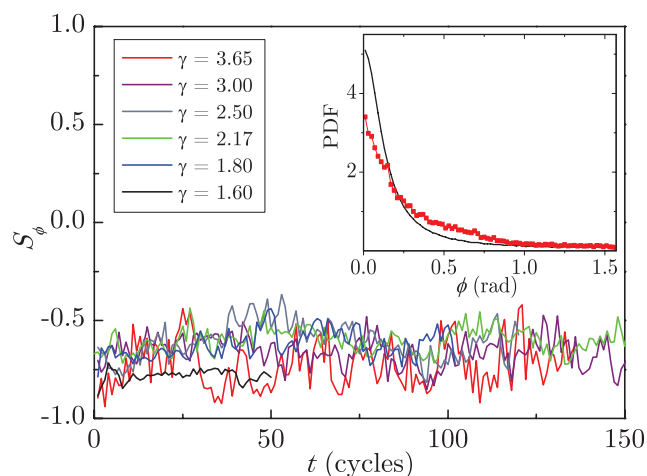
We use spherical coordinates to characterize fiber orientation, with θ the polar angle and ϕ the azimuthal angle The angle α is the angle between the x axis and the projection of the fiber onto the x-z plane (see Fig. 2), and is the angle that is directly measured when the laser sheer is oriented vertically. At a shear rate $\dot{\gamma}$, the evolution of ϕ and θ are given by

$$\tan \phi = \frac{1}{r \tan\left(\frac{\dot{\gamma}t}{r+1/r} + \delta\right)} \tag{1}$$

$$\tan \theta = \frac{Cr}{\sqrt{\cos^2 \phi + r^2 \sin^2 \phi}}, \tag{2}$$

where δ is the initial phase.[31]

These equations remain approximately valid for a suspensions at finite concentrations.[34] In this case, the orbit constant C has distribution $\mathcal{D}_t(C)$, with $\mathcal{D}_t(C)dC$ being the fraction of fiber at a time t that describes an orbit with a constant between C and $C + dC$. This distribution is evaluated by measuring the distributions of the projected angles α and ϕ at each time t, using a method described in the discussion section.

2.3 Orientation distribution

We extract the orientational probability distribution function (PDF) of ϕ from images like the one shown in Fig. 1c. From the PDF, we calculate an orientational order parameter $S_\phi = 1 - 2\langle\cos^2 \phi\rangle$, in which the angled brackets denote the ensemble average over a single image. For $c = 0.15$, $S_\phi(t)$ fluctuates around an average value $\overline{S_\phi} = -0.66 \pm 0.15$ independently of the strain amplitude (Fig. 3). This value is higher than the value of -0.77 expected from the Jeffery equations, signifying that the distribution of ϕ is slightly broader than predicted by Jeffery (see inset Fig. 3). Oscillatory shear does not change the distribution of ϕ; to within experimental resolution, it is the same as for the steady preshear.[28,35]

We extract the PDF of α from images like the ones shown in Fig. 1d, e, and again use the PDF to determine an orientational order parameter, in this case $S_\alpha(t) = 1 - 2\langle\cos^2 \alpha\rangle$, which quantifies the orientation in the x-z plane. In contrast to $S_\phi(t)$, $S_\alpha(t)$ generally increases with time, as shown in Fig. 4, signifying that fibers progressively align with the vorticity direction under periodic shear. This behavior was reported earlier.[22] Numerical simulations by Snook *et al.*[23] attribute the alignment of fibers to the confining effect of walls and to collisions between fibers. Figure 4, which shows $S_\alpha(t)$ for $c = 0.10$ at selected strain amplitudes, shows that $S_\alpha(t)$ does not vary at the lower strain amplitudes, but increases in the first 50 cycles for higher strain amplitudes. Similar behavior is observed at other volume fractions, although the strain amplitude necessary to cause significant orientation decreases with increasing the volume fraction.
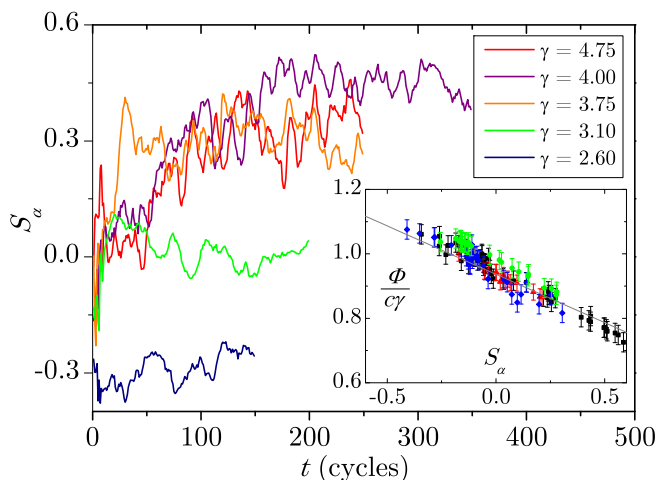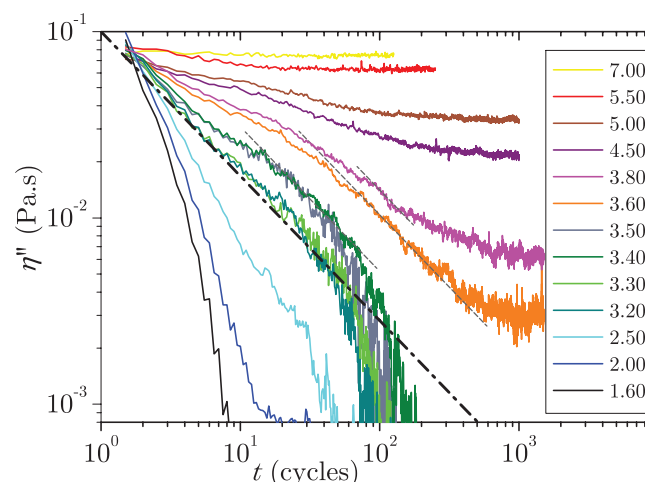
Fig. 4 Temporal evolution of S_α at $c = 0.10$ for selected strain amplitudes. **Inset**: $\Phi/(c\gamma)$ is expressed against S_α for samples in the initial state and in the steady state. The values of Φ are computed using eqn (6). The straight line is given by eqn (7), using B as a fitting parameter. Volume fractions: ■ $c = 0.20$, ▲ $c = 0.15$, ◆ $c = 0.10$, ● $c = 0.05$.

Fig. 5 Relaxation of the imaginary viscosity $\eta''(t)$ at $c = 0.10$. The dark straight line is the critical relaxation $t^{-\beta/\nu}$, as suggested by theory of APTs [10,36] The straight gray lines also show the critical relaxation $t^{-\beta/\nu}$ but shifted to later times.

2.4 Relaxation of the activity

Each cycle we record the apparent complex viscosity $\eta^*(t) = \eta'(t) + \imath\eta''(t)$, which typically evolves with time. As discussed in §7.4, the imaginary component $\eta''(t)$ serves as a quantitative measure of the activity of the suspension, that is, of the fraction or average degree of displacement of the fibers at time t. [15,22]

Figure 5 shows the relaxation of $\eta''(t)$ for selected strain amplitudes at a volume fraction of $c = 0.10$. The activity starts at a high level, set by the pre-straining protocol, and decreases with time, which means that the rods systematically move to positions that tend to decrease the overall number of collisions. At low strain amplitudes ($\gamma < 3.5$ for $c = 0.10$), η'' vanishes in less than a hundred cycles, which means that an absorbing state has been reached. At higher strain amplitudes, η'' decreases more slowly and eventually fluctuates around a finite value, which means that a fluctuating steady state has been reached.

Near the strain amplitude for which the total change $\Delta S_\alpha \equiv S_\alpha(\infty) - S_\alpha(0)$ is greatest, we observe one or more inflections in $\eta''(t)$. In Fig. 4, for example, we see that for $c = 0.10$, ΔS_α is greatest for $\gamma \approx 4$; in Fig. 5, we see inflections in $\eta''(t)$ around the same values. As we shall see, these inflections arise from emergence of nematic order as the fibers begin to align in the vorticity direction under the influence of the imposed periodic strain. The alignment of the fibers, which proceeds slowly under periodic strain, turns out to have a profound effect on the absorbing phase transition exhibited by this system.

As far as we know, these fiber suspensions constitute the first experimental system for which an absorbing phase transition controlled to a slowly-varying parameter such as nematic order.

3 Absorbing phase transition controlled by a time-dependent parameter

Theories of APTs suggest that the relaxation of the activity is controlled by a parameter Φ, defined in lattice models as the fraction of occupied sites.

For the case of non-colloidal suspensions, Φ is an *effective volume fraction*, defined by the volume swept out by the trajectories of all the fibers during a single shear cycle. That is, $\Phi = Nv/V$, where N the number of particles, V is the volume of the suspension, and v is the average volume swept out by particles during a period (Fig. 6). The volume swept out by an individual particle depends on its shape and orientation, and increases with the strain amplitude γ. Thus, Φ depends on the shape and orientation of particles, and increases with γ. In the absence of shear, Φ goes to zero. We define Φ in this way because we use Φ to characterize the probability that fibers collide with each other. In the absence of shear (and Brownian motion), the probability of a collision vanishes.

The definition of Φ used here differs from the effective volume fraction $\Phi'(t) = c + \Phi(t)$ we previously defined. [22] Scaling the dynamics of the suspension with Φ' or Φ is equivalent when dealing with a single value of concentration. However, the present study uses four different concentrations and we find that the suspension behavior is better captured by $\Phi(t)$

than by $\Phi'(t)$.

3.1 Effective volume fraction of a sphere suspension

As an example, we calculate the effective volume fraction of a suspension of spheres under oscillatory uniform shear flow with a strain amplitude γ and a frequency ω (eqn (3)), with U_x, U_y, U_z being the velocity component in the flow, gradient, and vorticity directions, respectively. Quantitatively, the velocity flow field is given by

$$U_x = y\gamma \sin\omega t, \qquad U_y = 0, \qquad U_z = 0. \qquad (3)$$

We define the cross-section σ of a sphere as its geometrical projection onto the plane perpendicular to the flow (Fig. 6a). The effective (additional) volume v swept out by a sphere is the circular cross section $\sigma(y, z)$ tilted back and forth in the x direction by the full peak-to-peak strain $2\gamma|y|$. Over one cycle, this volume is given by

$$v = 2\gamma \int |y|\, \sigma(y, z)\, dy\, dz. \qquad (4)$$

This volume v is represented on Fig. 6b for the first half of a cycle. For a suspension of spheres under periodic flow, performing the integral above leads to an effective volume fraction of

$$\Phi = \frac{Nv}{V} = \frac{2}{\pi}\gamma c. \qquad (5)$$

For a suspension of spheres, the effective volume fraction is proportional to the strain amplitude, the volume fraction, and a shape factor.

3.2 Effective volume fraction of a fiber suspension

The effective volume fraction Φ of a fiber suspension is the volume swept out by all the fibers during a cycle divided by the volume of the suspension. To measure the effective volume v that each fiber sweeps out during a cycle, we use a mean-field average that takes the orientations of the fibers into account: the cross section is averaged (*i*) over the orientation the fibers take when they describe an orbit C and (*ii*) over the distribution of orbits $\mathcal{D}_t(C)$.

The cross section σ_C of fibers is averaged over their orientations during an orbit characterized by orbit constant C: it is the accumulated projections onto the gradient-vorticity plane for a given orbit (dark shades in Fig. 6c-d). The effective volume v for the whole suspension is then expressed as an average over the distribution $\mathcal{D}_t(C)$ of Jeffery orbits

$$v = 2\gamma \int_C \left[\int_{y,z} |y|\, \sigma_C(y, z)\, dy\, dz \right] \mathcal{D}_t(C)\, dC \qquad (6)$$

The cross section σ_C becomes narrower and smaller as C decreases, which corresponds to greater orientation of fibers in
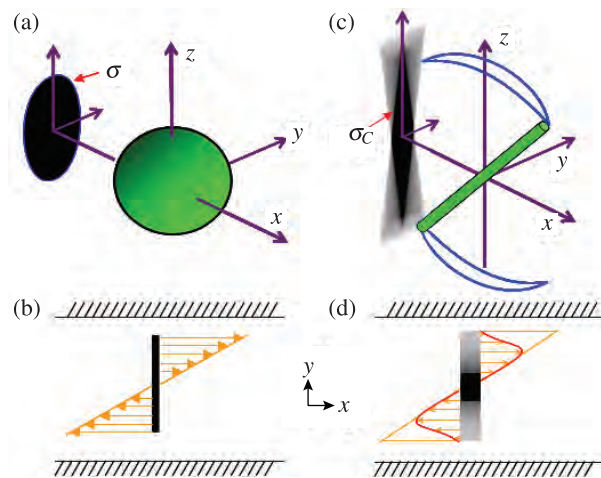
Fig. 6 a: Cross-section σ of a sphere. **b**: x-y view of the effective volume that will pass through σ during half a cycle. **c**: Cross-section σ_C of a Jeffery orbit with $C = 0.2$. σ_C is the accumulated projection of fibers describing that orbit. The gray scale reflects the non-homogeneous distribution of ϕ within a Jeffery orbit. **d**: x-y view of the effective volume that will pass through σ_C during half a cycle, weighted by the intensity of the cross-section.

the vorticity (z) direction. The effective volume also decreases as $\mathcal{D}_t(C)$ is shifted to the smaller values of C.

The distribution of orbits $\mathcal{D}_t(C)$ can be calculated at any time t, knowing the distribution of the projected angles $\phi(t)$ and $\alpha(t)$ at that time (see section 4.3). By expressing $\Phi = Nv/V$ as a function of S_α, we express the effective volume fraction Φ as a function of the strain amplitude, the volume fraction and the average value of the projected angle α

$$\Phi = c\gamma \left(2/\pi + B\langle \cos^2\alpha \rangle \right) \qquad (7)$$

The coefficient $B = 0.6 \pm 0.1$ is deduced from plotting $\Phi/(c\gamma)$ as a function of S_α (see inset, Fig. 4). Given this value, $\Phi \approx c\gamma$ for a suspension with a uniformly distributed projected angle α where $\langle \cos^2\alpha \rangle = \frac{1}{2}$, and $\Phi = \frac{2}{\pi}c\gamma$ for a nematic suspension where $\langle \cos^2\alpha \rangle = 0$.

From our measurements of the time-dependent distribution of α, we determine $\Phi(t)$ using eqn (7). In Fig. 7, we show typical plots of $\Phi(t)$ for different strain amplitudes for $c = 0.10$. The effective volume fraction can decrease by as much as 10% from its initial value as the fibers become more oriented. The evolution of the orientation shown in Fig. 4 has a significant effect on the probability that fibers collide. This 10% change in Φ is consistent with the change in collision rate reported by Singh *et al.*[9] It is small compared to the change induced by variation in the aspect ratio. As we shall see, however, even the change in average orientation can have dramatic consequences on the suspension dynamics.
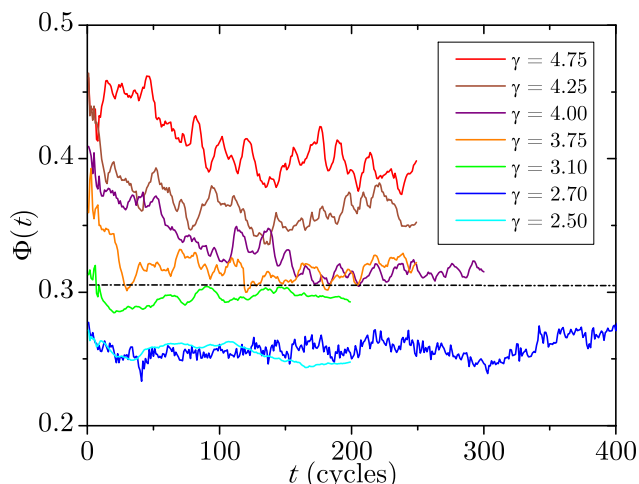
Fig. 7 Temporal evolution of the effective volume fraction $\Phi(t)$ at $c = 0.10$. The dotted line represents the critical effective volume fraction Φ_c, as discussed in section §4. Similar decay of Φ with time is observed for all volume fractions.

4 Relaxation of the activity: scaling with Φ

Experimentally, we find that the effective volume fraction Φ controls the absorbing phase transition in fiber suspensions under oscillatory shear. A critical threshold Φ_c separates absorbing states ($\Phi < \Phi_c$) for which activity vanishes, from fluctuating states ($\Phi > \Phi_c$) for which activity is remains finite and fluctuates around a steady state value. The critical threshold Φ_c is non-universal and must be experimentally determined.

Near the critical threshold where $\Phi \rightarrow \Phi_c$, theories of APTs suggest that the relaxation of the activity $\eta''(t)$ should, in analogy with continuous equilibrium phase transitions [10,36], follow a universal scaling law

$$\frac{\eta''(t)}{\eta_0''} = \left| \frac{\Phi}{\Phi_c} - 1 \right|^{\beta} \mathcal{F}_{\Phi}\left(\frac{t}{t_0} \left| \frac{\Phi}{\Phi_c} - 1 \right|^{\nu} \right) \qquad (8)$$

where β and ν are activity and time scaling exponents, and η_0'' is the initial value of η'' at t_0.

These exponents characterize the singularity observed around a critical point. As in equilibrium physics, systems that belong to the same universality class have identical exponents. [10,36] APT in systems that have a conserved number of particles belong to the Manna universality class [15,22,24] and the exponents are expected to be $\beta = 0.84$ and $\nu = 1.081$ in three dimensions. [10,36]

The scaling function $\mathcal{F}_{\Phi}$ is different above and below threshold but follows a power law $\mathcal{F}_{\Phi} \sim x^{-\beta/\nu}$ for both cases in the vicinity of Φ_c. Below Φ_c, the activity vanishes at long times: $\eta''(t = \infty) \equiv \eta_{\infty}'' = 0$. Above Φ_c, the steady state
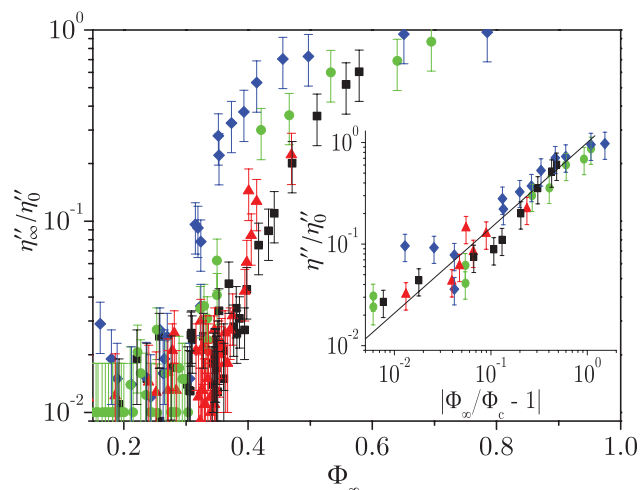
Fig. 8 Steady state activity against Φ_{∞}. Inset: Steady state activity against $|\Phi_{\infty}/\Phi_c - 1|$. Legend: ■ $c = 0.20$, ▲ $c = 0.15$, ♦ $c = 0.10$, ● $c = 0.05$, and —— $|\Phi_{\infty}/\Phi_c - 1|^{\beta}$.

activity is predicted to scale as

$$\eta_{\infty}'' = \eta_0'' \left| \frac{\Phi}{\Phi_c} - 1 \right|^{\beta} , \qquad (9)$$

such that activity vanishes continuously as $\Phi \rightarrow \Phi_c$ from above.

On both sides of the transition, the activity relaxation time τ, which is the longest correlation time in the system, is predicted to diverge according to a power law [26]

$$\tau = \frac{t_0}{\left| \frac{\Phi}{\Phi_c} - 1 \right|^{\nu}} . \qquad (10)$$

4.1 Measuring the critical exponents

To our knowledge, the exponent β of APT has been measured experimentally only in turbulent liquid crystals. [37] Here, we measure β by plotting η_{∞}''/η_0'' against Φ_{∞}, where Φ_{∞} is the final steady state value of Φ (see Fig. 7). The data are plotted in Fig. 8. Below Φ_c, the steady state activity is zero to within the noise. Above Φ_c, the steady state activity is finite and follows eqn (9) with $\beta = 0.84 \pm 0.04$. The critical value Φ_c exhibits a weak dependence on fiber concentration, which we discuss in §5, but is in the range of 0.3 to 0.4.

For $\Phi \rightarrow \Phi_c$, the relaxation time τ of the transient regime is expected to diverge according eqn (10). To obtain a correlation time for $\Phi < \Phi_c$, we model the time dependence of the data as a power law cut off by an exponential

$$\eta''(t) = \eta_0'' \frac{e^{(t_0 - t)/\tau}}{(t/t_0)^{\alpha'}} , \qquad (11)$$
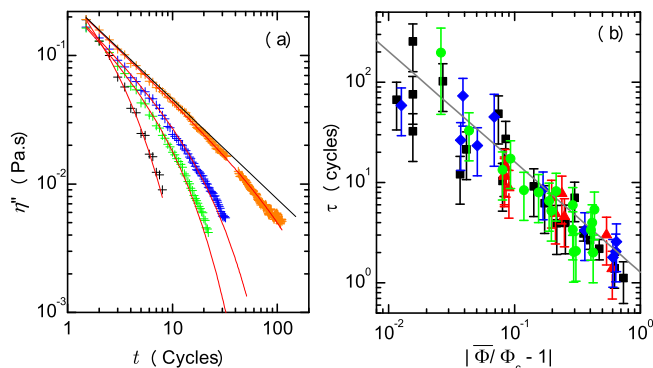
Fig. 9 (a) Decay of the activity for $c = 0.20$, fitted by quenched power law. Selected curves. The data curves are at $\gamma = 1.50$ (+), $\gamma = 1.95$ (+), $\gamma = 2.01$ (+) and $\gamma = 2.20$ (+). The fit curves (——) are done with eqn (11), leaving only τ as a fitting parameter. (b) Relaxation time τ vs $|\overline{\Phi} - \Phi_c|$ with $\overline{\Phi} = (\Phi_0 + \Phi_\infty)/2$. $c = 0.20$ (■), $c = 0.15$ (▲), $c = 0.10$ (♦), $c = 0.05$ (●), and $\left|\overline{\Phi}/\Phi_c - 1\right|^{-\nu}$ (——).

where $\alpha' = \beta/\nu$. Equation (11) captures the expected asymptotic power-law decay for $\Phi \to \Phi_c$. Figure 9(a) shows representative fits to eqn (11) at selected strain amplitudes for $c = 0.2$. The measured values of τ are plotted vs $\left|\overline{\Phi}/\Phi_c - 1\right|$, where $\overline{\Phi}$ is the average value of Φ during the decay, which varies by no more than a few percent for these data. We obtain our measurement of the time exponent from the slope in Figure 9(b), which gives $\nu = 1.1 \pm 0.1$.

Analysis of the data to measure τ for $\Phi > \Phi_c$ requires more care. Therefore, we defer that analysis until after we present the scaling of the data.

4.2 Scaling the data

Equation (8) suggests that all the data should collapse onto a pair of scaling curves $\mathcal{F}$, one for $\Phi > \Phi_c$ and another for $\Phi < \Phi_c$, if the data are plotted in terms of a rescaled activity A_R vs a rescaled time t_R

$$A_R = \frac{\eta''(t)}{\eta_0''} \left|\frac{\Phi}{\Phi_c} - 1\right|^{-\beta} \qquad (12)$$

$$t_R = \frac{t}{\tau} = \frac{t}{t_0} \left|\frac{\Phi}{\Phi_c} - 1\right|^{\nu} , \qquad (13)$$

In a previous publication we showed that such scaling is indeed observed near Φ_c.[22] Here we present a somewhat different scaling analysis, consistent with the previous scaling, that extends the scaling to a larger range of $|\Phi - \Phi_c|$ and in the process shows more precisely under what conditions scaling breaks down.

We already know that for $\Phi > \Phi_c$, the long-time activity η_∞''/η_0'' scales as $|\Phi/\Phi_c - 1|^{\beta}$ and that for $\Phi < \Phi_c$, $\eta_\infty'' \to 0$.

To focus on the temporal scaling of the activity, we subtract off the log-time asymptotic part η_∞'', which is given by eqn (9). This allows us to more directly compare the temporal scaling of the activity above and below criticality. Therefore, we examine the scaling of a reduced activity $\delta A_R(t)$ the form

$$\delta A_R(t) = \frac{\eta''(t) - \eta_\infty''}{\eta_0'' - \eta_\infty''} e^{-\left|\frac{\Phi_0}{\Phi_c} - 1\right|^{\nu}} \qquad (14)$$

$$= \left|\frac{\Phi}{\Phi_c} - 1\right|^{\beta} \mathcal{G}_\Phi\left(\frac{t}{t_0} \left|\frac{\Phi}{\Phi_c} - 1\right|^{\nu}\right) . \qquad (15)$$

In this equation, Φ_0 is the initial value of Φ at t_0, and the exponential factor takes into account the decay of activity that occurs during the first time step before we start recording data. This is a consequence of the discrete nature of the time t, which implies that the reduced time t_R starts at a the finite value $|\Phi_0/\Phi_c - 1|^{\nu}$.

Figure 10 shows $\delta A_R(t)$ plotted vs t_R for data taken below and above the phase transition. In these experiments, nematic order builds up during the measurements, as shown in Fig. 7, causing $\Phi(t)$ to decrease with time. We have taken this time dependence into account in the data plotted in Fig. 10 by using the measured time-dependent $\Phi(t)$. Such a procedure should be valid in the quasistatic limit where the variation of $\Phi(t)$ occurs on a time scale longer than the activity relaxation time τ. Examining Fig. 10, we see that the scaled data, both above and below the transition, are well described by a power law quenched by an expoential

$$\mathcal{G}_\Phi(t_R) = \frac{e^{-t_R}}{t_R^{\alpha'}} , \qquad (16)$$

with $\alpha' = 0.75 \pm 0.05$, which further justifies our use of eqn (11) in the previous section. This remarkable scaling means that the relaxation time τ diverges both above and below the transition according to (eqn 10).

4.3 Data that do not scale

In all of our experiments Φ evolves in time as nematic order among the fibers builds up. In some cases, this means that the system starts in the fluctuating state where the initial effective volume fraction is above the critical value ($\Phi_0 > \Phi_c$) but crosses over into the absorbing state and ends with $\Phi_\infty < \Phi_c$. Because τ diverges at Φ_c, this means that any time variation in $\Phi(t)$ will necessarily occur on a time scale shorter than τ very near Φ_c: the quasistatic condition assumed in the previous section will be violated in these cases.

Figure 11 shows data for $\Phi(t) > \Phi_c$ for cases where $\Phi_0 > \Phi_c$, but $\Phi_\infty < \Phi_c$. Data up to the time where $\Phi(t)$ crosses Φ_c are shown. Obvious deviations from scaling are apparent. Interestingly, the data all fall on or *below* the expected scaling curve given by eqn (16), indicating faster than
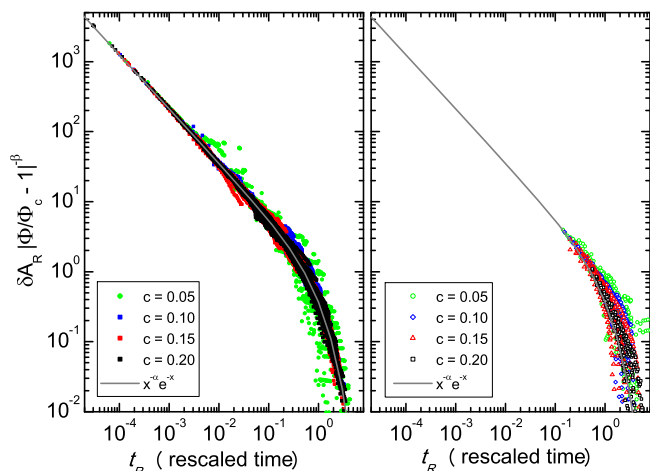
Fig. 10 Scaling of the viscosity ratio $A_R(t)$ for $c = 0.05, 0.10, 0.15,$ and 0.20. (a) Below ($\Phi < \Phi_c$) and (b) above ($\Phi > \Phi_c$) the phase transition. The gray continuous line is given by $a_R = t_R^{-\alpha'} e^{-t_R}$. The scaling behavior encompasses all fiber concentrations and all shear rates studied. In general, the data above the transition correspond to experiments with higher strain, higher fiber concentration, and less fiber alignment.
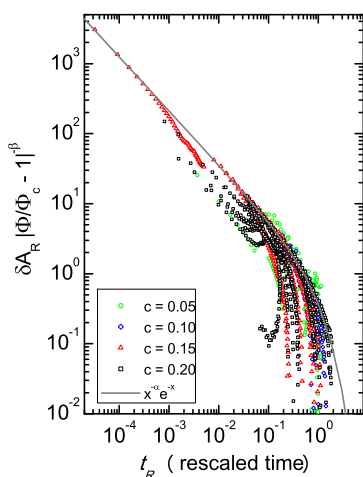
Fig. 11 Scaling curves of the viscosity ratio $A_R(t)$ for $c = 0.05, 0.10, 0.15,$ and 0.20 for the the case where $\Phi(0) > \Phi_c$ but crosses over into the absorbing state and ends with $\Phi_\infty < \Phi_c$. The gray continuous line is given by $a_R = t_R^{-\alpha'} e^{-t_R}$.

expected relaxation. This is because the temporal variation in $\eta''(t)$ is dominated by the time dependence of $\Phi(t)$, which in this regime becomes *faster* that the expected relaxation time τ for the activity.

Once $\Phi(t)$ passes below Φ_c, the quasistatic condition is rapidly recovered and the data once again begins to decay as
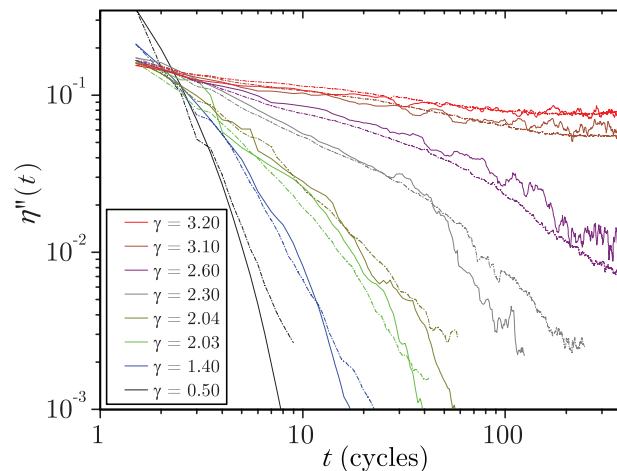

Fig. 12 (—): Temporal decay of $\eta''(t)$ at $c = 0.20$, for selected strain amplitudes. (— – —): Decay calculated using $\Phi(t)$, eqn (9)-(10) and the universal exponents $\beta = 0.84$ and $\nu = 1.081$. The critical value is $\Phi_c = 0.39 \pm 0.02$ at this volume fraction.

$t^{-\alpha'} = t^{-\beta/\nu}$, because the effective volume fraction is very near Φ_c. In Fig. 5, we show three such curves with dashed gray lines showing the power-law decay. Because the time at which this happens is delayed, we must replace t_0 with t_1, the time at which the data emerges below Φ_c and and η''_0 with η''_1, the corresponding viscosity at this time, in order to place the data on the scaling curve. After this, the relaxation continues along the scaling curve. These data are included in Fig. 10(a). In discussing the time dependence of these results, particularly as it relates to the observed scaling, we emphasize that time is measured in units of the the period of oscillation: 1 period, 2 periods, *etc*. Halving or double the oscillation frequency has no effect on the data so long as $Re \ll 1$.

4.4 Relaxation of $\eta''(t)$

In the previous sections we have shown how the data can be scaled using the time-dependent effective volume fraction $\Phi(t)$. It is also interesting to see how this analysis describes the raw data $\eta''(t)$ to better understand how the features observed in $\eta''(t)$ are captured by our analysis.

Figure 12 shows representative data for $c = 0.20$, which illustrates how the analysis works. The inflection in the data observed at intermediate strain amplitudes is a consequence of the nematic order that builds up under oscillatory shear in a confined geometry.[23] The model captures these kinds of features and gives a reasonably good description of the data.
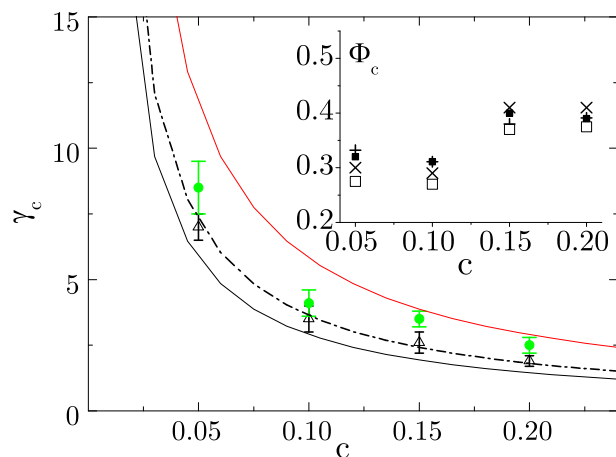
Fig. 13 Relation between the critical strain amplitude and the concentration, using $\Phi_c = 0.35$. Initial γ_c ($\triangle$), final γ_c (●), prediction of γ_c with the initial distribution of orbit (— · —), maximal value of γ_c. (—), minimal value of γ_c (—). **Inset:** Measures of Φ_c against the volume fraction c. Φ_c is measured at the steady state (+), in the initial state (□), chosen to fit the whole experiment (×) or chosen to in order to rescale the curves (■).

5 Critical strain amplitude

Figure 13 shows the dependence of the critical strain γ_c and the critical effective volume fraction Φ_c (inset) on concentration. Recalling from §2.1 that all the data are above the overlap concentration $c^\star \approx 0.01$ but that only the highest two concentrations are clearly in the concentrated regime $c^{\star\star} \approx 0.1$, the data suggest that $\Phi_c = 0.30 \pm 0.02$ in the semidilute regime and a bit larger 0.40 ± 0.02 in the concentrated regime. This may indeed be the case but at present there is no theoretical understanding of what Φ_c should be.

The concentration dependence of the critical strain γ_c is also shown. It is consistent with $\gamma_c = \mathcal{O}(1/c)$.

6 Conclusion

We studied the dynamics of a concentrated suspension of rods under periodic shear at four different volume fractions ranging from 0.05 to 0.2. For strain amplitudes near unity, the orientation of the fibers evolves with time towards a steady state in which the fibers orient substantially along the vorticity axis. The evolution and dynamics of the fibers slows as the fibers orient along the vorticity axis making collisions less like. We quantitatively describe this effect by measuring the cross-section of the fiber under shear and by defining an effective volume fraction $\Phi(t)$ that takes this cross section into account. For low values of the effective volume fraction, the suspension finds a state in which all the fibers have periodic

reversible trajectories. Above a critical threshold, the suspension cannot find such a state and fluctuations remain. These fluctuations as well as the transient durations, are linked by critical exponent to the effective volume fraction. We found that the mechanism behind this transition is similar to the one observed in sphere suspensions.

The effective volume fraction $\Phi \propto \gamma c$ is the equivalent under periodic shear of an ideal collision rate. The ratio of Φ over γc is a time-dependent scalar that represent the average orientation of the suspension. Φ is expressed simply as a function of S_α, the orientation parameter of the projected angle α: the effective volume fraction can be measured each period by taking snapshot of the flow-vorticity plane. We showed that the temporal decay in the effective volume fraction, which is due to the evolution of the orientation distribution, is independent of the strain amplitude or volume fraction.

At sufficiently large strain amplitudes, typically in the range of $\gamma \sim 3 - 9$, the effective volume fraction $\Phi \propto \gamma c$ always exceeds the critical volume fraction $\Phi_c \sim 0.3 - 0.4$. In this high strain amplitude limit, the fibers continue to collide and the system never reaches a reversible steady state. Under these conditions, the nematic order diminishes significantly, as discussed in a previous study.[22] In no case do we observe larger scale structures, as observed for some other rod-like systems.[38]

Finally, we note that in an important numerical study by Snook *et al.*,[23] the alignment of fibers in the vorticity direction was found to be strongly influenced by the confining walls of the shear device. In our experiments, the distance between the confining walls of the Couette device was $1.5L$, well within the narrow-gap regime defined by Snook *et al.*.[23] In future studies, it would be interesting to investigate the effect of a wider gap, as well as the effect of varying the aspect ratio of the rods.

7 Material and methods

7.1 Solution

The continuous phase of the suspension is a mix of Triton-X100, Zinc Chloride ($ZnCl_2$), and a hydrochloric acid (HCl) solution ($pH = 0$). Its real viscosity is $\eta_0 = 1$ Pa-s and its density is $\rho = 1.129$ gm/ml. The density is adjusted by adding small amounts of either $ZnCl_2$ or Triton until it perfectly matches the density of the fiber at the experiments temperature ($22.0°C$).

7.2 Strain protocol

The suspensions are placed between concentric cylinders (gap $g = 2.2$ mm) of a transparent thermostated Couette cell. The inner cylinder ($R = 25$ mm), driven by a Paar Physica
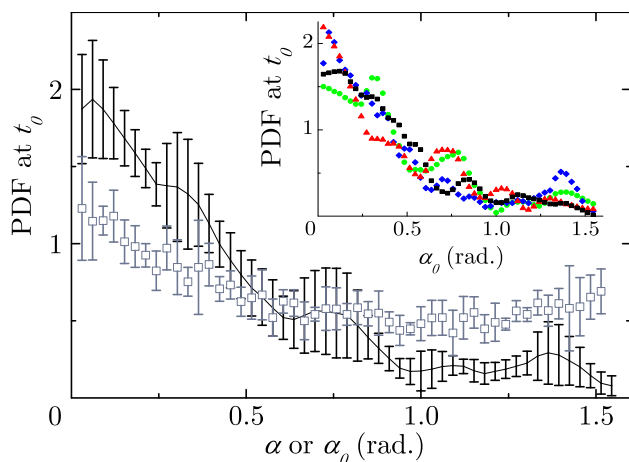
Fig. 14 Comparison between the distribution of α ($\square$) and α_0 (—), at the start of experiment. This dataset is an average over the four volume fraction tested. The distribution of α_0 is skewed toward the smallest values but remain broad. **Inset**: Dataset for each volume fraction, $c = 0.20$ ($\blacksquare$), $c = 0.15$ ($\blacktriangle$), $c = 0.10$ ($\blacklozenge$), $c = 0.05$ ($\bullet$).

Fig. 15 Inset: Activity $A(t)$ measured from tracer fibers, as defined by eqn (19), presented for $c = 0.20$. $\gamma = 1.6$ ($\blacksquare$), $\gamma = 2.10$ ($\blacksquare$), $\gamma = 2.35$ ($\blacksquare$), $\gamma = 2.5$ ($\blacksquare$), and $\gamma = 3.2$ ($\blacksquare$), and $t^{-0.75}$ (— · —). Main Graph: Ratio $A(t)/\eta''$, which evaluate the relative evolution of these two activity measurements. $c = 0.20$ (—), $c = 0.15$ (—), $c = 0.10$ (—)

MCR300 rheometer-head, is rotated back and forth through a small angle ψ to produce an oscillatory time-dependent strain $\gamma \sin \omega t$ with angular frequency ω and strain amplitude $\gamma = \psi R/g$. Given the aspect ratio $L/D = 11$, the necessary strain amplitude to achieve a full period is 45. In our experiments, the strain is limited to 15, which implies that the fiber trace only a fraction of their Jeffery orbits.
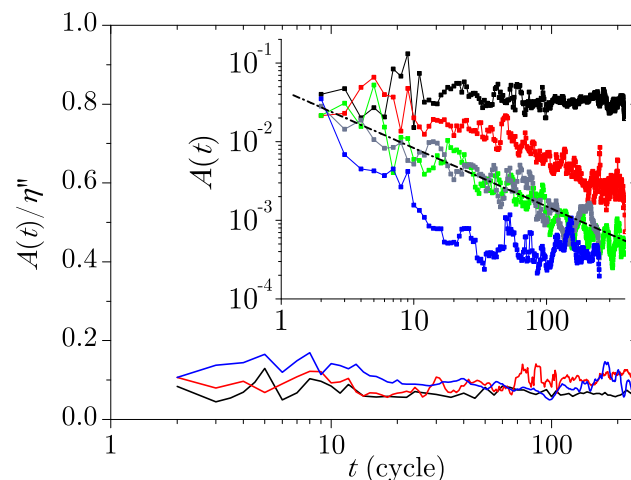
7.3 Extraction of the distribution $\mathcal{D}_t(C)$

We evaluate the distribution $\mathcal{D}_t(C)$ of orbit C using the distribution at t of α, the angle of the projected fiber on the x-z plane and the distribution of azimuth ϕ, which is a constant throughout all our experiments. When a fiber describe a Jeffery orbit, its projected angle α varies between $\pi/2$ and α_0, the smallest angle a fiber has with the x axis when it describes a Jeffery orbit (eqn (17) and eqn (18)).

$$\tan(\alpha_0) = \frac{1}{Cr} \qquad (17)$$

$$\tan(\alpha) = \tan(\alpha_0)\sqrt{1 + r^2 \tan^2(\phi)} \qquad (18)$$

Since the distribution of ϕ is constant of the system, the distribution of α_0 (Fig. 14) is deduced from the observed distribution of α. $\mathcal{D}_t(C)$ (the distribution of C) is then taken from the distribution of α_0 using eqn (17).

7.4 Comparison between particle tracking and apparent imaginary viscosity

The activity can be measured by the apparent complex viscosity, whose imaginary (out-of-phase) component η'' is a function of the particles collisions. It can also be measured with the mean square angular displacement of the $N(t)$ tracer fibers from t to $t + 1$ (eqn (19)).

$$A(t) = \frac{1}{N(t)} \sum_{i=0}^{n} |\alpha_i(t) - \alpha_i(t-1)|^2, \qquad (19)$$

The apparent viscosity has a better signal-over-noise ratio than the mean square displacement we can obtain from tracking, since the measurement is averaged over the whole sample instead of the 20 to 50 fiber we can capture in a frame (there is around 10^6 fiber in a suspension, yet a snapshot capture less than 50 of them). Fig. 15 shows that the ratio between the mean square angular displacement $A(t)$ and η'' is constant throughout the experiment, showing that these two activity measurement are equivalent.

Acknowledgements

References

1 R. Elgaddafi, R. Ahmed, M. George and F. Growcock, *J. Petrol. Sci. Eng.*, 2012, **84-85**, 20–28.

2 H. Savastano, S. F. Santos, M. Radonjic and W. O. Soboyejo, *Cement Concrete Comp.*, 2009, **31**, 232–243.

3 A. Kabla and L. Mahadevan, *J. Roy. Soc. Interface*, 2007, **4**, 99 –106.

4 J. Dupire, M. Socol and A. Viallat, *Proc. Nat. Acad. Sci. USA*, 2012, **109**, 20808–20813.

5 C. J. Petrie, *J. Non-Newt. Fluid Mech.*, 1999, **87**, 369–402.

6 S. Mueller, E. W. Llewellin and H. M. Mader, *Proc. Roy. Soc. A: Math. Phys.*, 2010, **466**, 1201–1228.

7 S. B. Lindstrom and T. Uesaka, *J. Chem. Phys.*, 2008, **128**, 024901.

8 C. Servais, J.-A. E. Manson and S. Toll, *J. Rheol.*, 1999, **43**, 991–1004.

9 V. Singh, D. L. Koch and A. D. Stroock, *Langmuir*, 2011, **27**, 11813–11823.

10 S. Lubeck, *Int. J. Mod. Phys. B*, 2004, **18**, 3977–4118.

11 M. P. Ciamarra, P. Richard, M. Schröter and B. P. Tighe, *Soft Matter*, 2012, **8**, 9731.

12 J. R. Happel and H. Brenner, *Low Reynolds Number Hydrodynamics: With Special Applications to Particulate Media*, Springer, 1965.

13 D. J. Pine, J. P. Gollub, J. F. Brady and A. M. Leshansky, *Nature*, 2005, **438**, 997–1000.

14 B. Metzger and J. E. Butler, *Phys. Rev. E*, 2010, **82**, 051406.

15 L. Corté, P. M. Chaikin, J. P. Gollub and D. J. Pine, *Nat Phys*, 2008, **4**, 420–424.

16 B. Metzger and J. E. Butler, *Phys. Fluids*, 2012, **24**, 021703.

17 G. I. Menon and S. Ramaswamy, *Phys. Rev. E*, 2009, **79**, 061108.

18 P. Arp and S. Mason, *J. Coll. Int. Sci.*, 1977, **59**, 378.

19 A. Okagawa and S. Mason, *Science*, 1973, **181**, 159–161.

20 A. Okagawa, G. Ennis and S. Mason, *Can. J. Chem.*, 1978, **56**, 2815–2823.

21 G. Ennis, A. Okagawa and S. Mason, *Can. J. Chem.*, 1978, **56**, 2824–2832.

22 A. Franceschini, E. Filippidi, E. Guazzelli and D. J. Pine, *Phys. Rev. Lett.*, 2011, **107**, 250603.

23 B. Snook, E. Guazzelli and J. E. Butler, *Phys. Fluids*, 2012, **24**, 121702–121702–7.

24 L. Corté, S. J. Gerbode, W. Man and D. J. Pine, *Phys. Rev. Lett.*, 2009, **103**, 248301.

25 H. Hinrichsen, *Adv. Phys.*, 2000, **49**, 815.

26 M. Henkel, H. Hinrichsen and S. Lübeck, *Non-equilibrium phase transitions: Absorbing phase transitions*, Springer, 2008, p. 385.

27 C. Reichhardt and C. J. O. Reichhardt, *Phys. Rev. Lett.*, 2009, **103**, 168301.

28 F. Folgar and C. L. Tucker, *J. Reinf. Plast. Comp.*, 1984, **3**, 98–119.

29 A. Salahuddin, J. Wu and C. K. Aidun, *J. Fluid Mech.*, 2012, **692**, 153–182.

30 J. C. Crocker and D. G. Grier, *J. Coll. Int. Sci.*, 1996, **179**, 298–310.

31 F. P. Bretherton, *J. Fluid Mech.*, 1962, **14**, 284–304.

32 G. Jeffery, *Proc. Roy. Soc. Lond. Ser. A*, 1922, **102**, 161–179.

33 C. A. Stover and C. Cohen, *Rheologica Acta*, 1990, **29**, 192–203.

34 M. Fiahnama, D. L. Koch and E. S. Shaqfeh, *Phys. Fluids*, 1995, **7**, 487–506.

35 C. A. Stover, D. L. Koch and C. Cohen, *J. Fluid Mech.*, 1992, **238**, 277–296.

36 S. B. Lee, *Phys. Rev. E*, 2012, **85**, 022101.

37 K. A. Takeuchi, M. Kuroda, H. Chaté and M. Sano, *Phys. Rev. E*, 2009, **80**, 051116.

38 S. Lin-Gibson, J. Pathak, E. Grulke, H. Wang and E. Hobbie, *Phys. Rev. Lett.*, 2004, **92**, 048302.